



## Crystallization behavior in BaO–CaO–SiO<sub>2</sub>–Al<sub>2</sub>O<sub>3</sub>–B<sub>2</sub>O<sub>3</sub> glass sealants for SOFCs: Influence of SiO<sub>2</sub> and B<sub>2</sub>O<sub>3</sub> content

Andrey O. Zhigachev<sup>a,\*</sup> , Irina I. Zverkova<sup>a</sup>, Denis S. Katrich<sup>a</sup>, Nailya S. Saetova<sup>b</sup> ,  
Sergey I. Bredikhin<sup>a</sup>

<sup>a</sup> Osipyan Institute of Solid State Physics RAS, Chernogolovka, 142432, Russia

<sup>b</sup> Vyatka State University, Kirov, 610000, Russia

### ARTICLE INFO

Handling Editor: Dr Mehran Rezaei

#### Keywords:

SOFC  
Glass sealant  
XRD  
Crystallization  
Raman spectroscopy

### ABSTRACT

This study investigates the crystallization behavior of 0.17BaO–0.17CaO–0.05Al<sub>2</sub>O<sub>3</sub>–(0–0.09)B<sub>2</sub>O<sub>3</sub>–(0.61–0.52)SiO<sub>2</sub> glass sealants for solid oxide fuel cell systems, a critical factor influencing long-term performance. Isothermal heat treatments (850–950 °C) revealed that higher boron oxide (B<sub>2</sub>O<sub>3</sub>) content inhibits bulk crystallization. Walstromite (Ca<sub>2</sub>BaSi<sub>3</sub>O<sub>9</sub>) was the primary crystalline phase in most compositions, with minor hexacelsian (BaAl<sub>2</sub>Si<sub>2</sub>O<sub>8</sub>). Notably, the 0.06 B<sub>2</sub>O<sub>3</sub> composition exhibited significant pseudowollastonite (CaSiO<sub>3</sub>) crystallization. Simulated sealing and operating conditions induced markedly different crystallization, particularly in high-boron compositions, with itsite ((Ba<sub>2</sub>Ca(BSi<sub>2</sub>O<sub>7</sub>)<sub>2</sub>)<sub>2</sub>) emerging as the dominant phase after 100 h. In-situ Raman spectroscopy showed limited sensitivity to ongoing crystallization at operating temperatures, suggesting slower surface crystallization compared to bulk crystallization.

### 1. Introduction

Fuel cells are electrochemical devices that directly convert the chemical energy of a fuel into electrical energy and heat through the electrochemical combination with an oxidant [1–3]. This direct conversion, bypassing combustion, yields superior energy efficiency compared to traditional power generation devices [4–6]. Solid oxide fuel cells (SOFCs), employing oxygen-conducting ceramic membranes, are promising for stationary, large-scale electricity generation and combined cooling, heat, and power (CCHP) applications [7]. Unlike low-temperature proton exchange membrane fuel cells, SOFCs can operate on carbon monoxide and hydrocarbon fuels, as well as pure hydrogen. This fuel flexibility stems from their high operating temperatures, enabling internal fuel reforming [8–11]. Furthermore, SOFCs exhibit high tolerance to fuel impurities, such as sulfur [12].

The high operating temperatures of SOFCs impose design limitations, particularly on material selection. Matching the coefficients of thermal expansion (CTE) among the electrolyte, electrode, and interconnect components is crucial [4,13,14]. SOFC materials must also maintain stable key properties, chemical stability, and phase composition during long-term exposure to oxidizing and reducing environments, typically exceeding 600 °C [15–17]. High operating temperatures also complicate

sealing, a critical aspect for ensuring the efficiency, stability, and long-term performance of SOFCs. These elevated temperatures, exceeding 600 °C even in intermediate-temperature SOFCs (IT-SOFCs), preclude the use of organic-based seals, limiting the viable options primarily to glasses and glass ceramics, although metal- and mica-based compliant seals are sometimes employed [18,19].

Current SOFC sealant research focuses primarily on silicate, aluminosilicate, and, especially for intermediate-temperature SOFCs (IT-SOFCs), borosilicate glass systems [18,20–22]. The performance characteristics of sealants based on these systems can be finely tuned through strategic selection of chemical composition and precisely controlled processing parameters.

Barium aluminosilicate glasses are widely investigated and used as SOFC sealants. These systems typically include a fluxing agent to improve glass flow and lower the softening point [23,24], alongside modifier and intermediate oxides to tailor crystallization and the CTE [25–29]. Calcium oxide and barium oxide are commonly employed as network modifiers due to the potential formation of crystalline phases with desirable CTE values upon crystallization, such as hexacelsian BaAl<sub>2</sub>Si<sub>2</sub>O<sub>8</sub> ( $9\text{--}13 \times 10^{-6} \text{ K}^{-1}$ ), BaSiO<sub>3</sub> ( $9\text{--}13 \times 10^{-6} \text{ K}^{-1}$ ), and walstromite Ca<sub>2</sub>BaSi<sub>3</sub>O<sub>9</sub> [25]. Careful adjustment of the BaO/CaO ratio and optimized thermal treatment allow control over the resulting

\* Corresponding author.

E-mail address: [zhigachev@issp.ac.ru](mailto:zhigachev@issp.ac.ru) (A.O. Zhigachev).

<https://doi.org/10.1016/j.ijhydene.2025.150298>

Received 18 April 2025; Received in revised form 20 June 2025; Accepted 1 July 2025

Available online 3 July 2025

0360-3199/© 2025 Hydrogen Energy Publications LLC. Published by Elsevier Ltd. All rights are reserved, including those for text and data mining, AI training, and similar technologies.

glass-ceramic sealant's CTE. Barium-calcium aluminosilicate (BCAS) glasses and glass-ceramic sealants are considered promising for SOFC sealing [30].

Developing suitable glasses and glass-ceramics for SOFC seals is a challenging task, necessitating careful consideration of several critical properties. These essential properties include, but are not limited to: thermomechanical compatibility with other SOFC components; predictable crystallization behavior; suitable high-temperature rheological properties; strong adhesion to both interconnect and electrolyte materials; and sustained stability of composition and properties over extended operating periods.

Crystallization behavior is paramount for seal performance. Crystallization in SOFC seals is virtually unavoidable due to prolonged exposure to operating temperatures, which are significantly above the glass transition temperature. A low crystallization rate during sealing and operation is generally preferred, as it preserves a ductile amorphous phase at operating temperatures, thereby mitigating potential thermomechanical stresses and ensuring air-tight interface with other components of the SOFC. However, with some degree of crystallization is unavoidable, whether the resulting crystalline phases are ultimately beneficial or detrimental depends on both the initial glass composition and the specific thermal treatment conditions employed.

Excessive crystallization at the operating temperature can compromise seal performance by transforming the entire seal into a rigid, fully crystalline material. Even partial crystallization can be detrimental if it leads to the formation of phases with coefficients of thermal expansion (CTEs) that deviate significantly from the desired CTE range ( $9\text{--}13 \times 10^{-6} \text{ K}^{-1}$ ). Specific examples of commonly observed phases that negatively impact the thermomechanical behavior and long-term stability of BCAS seals include monoclinic  $\text{BaAl}_2\text{Si}_2\text{O}_8$  ( $2.3 \times 10^{-6} \text{ K}^{-1}$ ) and wollastonite  $\text{CaSiO}_3$  ( $4.9 \times 10^{-6} \text{ K}^{-1}$ ) [25].

Crystallization can enhance seal performance if it includes formation of phases with suitable CTEs, such as hexacelsian  $\text{BaAl}_2\text{Si}_2\text{O}_8$  or walsstromite  $\text{Ca}_2\text{BaSi}_3\text{O}_9$  [25]. Even if the CTE of the crystallizing phase falls slightly outside the ideal range, it can still be beneficial if it shifts the overall CTE of the resulting glass-ceramic composite closer to the target CTE range.

The significance of crystallization behavior in SOFC seals is well-documented in the literature, with numerous studies focusing on crystallization in  $\text{BaO-SiO}_2\text{-Al}_2\text{O}_3\text{-B}_2\text{O}_3$  and  $\text{CaO-SiO}_2\text{-Al}_2\text{O}_3\text{-B}_2\text{O}_3$  systems [24,25,31–35]. BCAS glasses, containing both BaO and CaO, are recognized as promising sealants for SOFC applications [30]. However, comprehensive crystallization data for the BCAS system remains limited, partly due to the extensive range of viable compositions. Notable among the publications on BCAS sealants is [25], which provides a detailed analysis of crystallization in a BCAS seal, although this analysis is limited to a single composition, restricting the generalizability of its findings.

This study aims to address, in part, the existing knowledge gap by investigating the crystallization behavior of BCAS glass sealants with varying boron oxide content. While silica forms the main network in these sealants, boron oxide is used as a partial substitute to tailor key properties. Replacing silica with boron oxide typically lowers the glass-transition temperature, softening, and melting points. Boron oxide also improves BCAS glass flux and wetting, but can reduce chemical stability, particularly in humid environments, and may promote the formation of low-CTE borate phases.

Specifically, the  $0.17\text{BaO-}0.17\text{CaO-}0.05\text{Al}_2\text{O}_3\text{-(}0\text{--}0.09\text{)B}_2\text{O}_3\text{-(}0.61\text{--}52\text{)SiO}_2$  compositional range is examined in the study. The compositional range was selected based on preliminary experiments indicating that the chosen modifier/intermediate oxide ratio promoted the formation of desirable crystalline phases. Furthermore, the network former/modifier oxide ratio provided a suitable balance between crystallization rate and melt viscosity for convenient processing. The upper limit for boron concentration was determined by the potential for forming undesirable borate crystalline phases.

Previous research [36] has demonstrated that the high-temperature sealant behavior within this range can be controlled through adjustments to the silica and boron oxide concentrations. However, the crystallization data presented in that study was limited in scope. The present investigation provides a more detailed and comprehensive analysis of crystallization behavior across this compositional range. It encompasses data on the extent of crystallization and the fractions of crystalline phases following isothermal heat treatments and simulated sealing and operating conditions, including long-term exposure to operating temperatures. Diffraction data is complemented by electron microscopy images, calorimetric measurements, and in-situ Raman spectroscopy.

## 2. Materials and methods

This study investigated  $\text{BaO-CaO-Al}_2\text{O}_3\text{-SiO}_2\text{-B}_2\text{O}_3$  glass sealants for solid oxide fuel cells, systematically varying  $\text{SiO}_2$  and  $\text{B}_2\text{O}_3$  content while maintaining constant molar fractions of BaO, CaO, and  $\text{Al}_2\text{O}_3$ . A series of glass formulations (Table 1) were prepared with  $\text{SiO}_2$  ranging from 52 to 61 mol% in 3 mol% increments, and  $\text{B}_2\text{O}_3$  adjusted from 0 to 9 mol%. The molar proportions of BaO, CaO, and  $\text{Al}_2\text{O}_3$  were based on the authors' preliminary research optimizing these components for SOFC sealing.

Glass sealants were prepared from barium carbonate ( $\text{BaCO}_3$ ), calcium carbonate ( $\text{CaCO}_3$ ), alumina ( $\text{Al}_2\text{O}_3$ ), silica ( $\text{SiO}_2$ ), and boron oxide ( $\text{B}_2\text{O}_3$ ) powders. All powders, supplied by Chemcraft (Russia) with >99.9 wt% purity, were stoichiometrically weighed and thoroughly mixed before loading into a platinum crucible. Platinum was chosen to minimize melt-crucible interactions, particularly with high-boron compositions. The mixture was melted in an LHT 02/17 LB furnace (Nabertherm, Germany) at  $1500 \text{ }^\circ\text{C}$ , using a  $300 \text{ }^\circ\text{C/h}$  heating rate and a 1 h dwell at peak temperature. The melt was quenched in room-temperature distilled water. The resulting glass frit was milled to  $\sim 5\text{--}10 \text{ }\mu\text{m}$  median particle size using a Pulverisette 2 zirconia mortar grinder (Fritsch, Germany). Particle size distribution was confirmed with a Fritsch Analysette 22 NeXT laser diffraction analyzer to eliminate confounding effects on high-temperature behavior.

A Misura 3 HSML hot stage microscope (ESS, Italy) was used to assess high-temperature sealant behavior. Ground sealant powder was compacted into  $\sim 3 \text{ mm} \times 3 \text{ mm}$  rectangular samples. Consistent powder mass ensured minimal thickness influence on measurements. Samples were heated from room temperature to  $1100 \text{ }^\circ\text{C}$  at  $2 \text{ }^\circ\text{C/min}$  and cooled. Images were acquired during heating and analyzed with the instrument's software to determine sintering, softening, sphere, half-sphere, and flow temperatures.

Sealants were thermally treated for 1.5 h at  $750\text{--}950 \text{ }^\circ\text{C}$  ( $50 \text{ }^\circ\text{C}$  increments) on inert zirconia substrates to prevent reactions. A separate experiment assessed crystallization during prolonged exposure. Sealants were heat-treated for 1.5 h at HSM-determined sealing temperatures, cooled by  $100 \text{ }^\circ\text{C}$  to simulate operating temperatures, and held for 1 h and 100 h.

The phase composition and crystallinity of the sealants were characterized by X-ray diffraction (XRD) after casting and thermal treatment designed to simulate sealing and operating conditions. XRD patterns were acquired using a Smartlab SE diffractometer (Rigaku, Japan) with a copper X-ray tube in Bragg-Brentano geometry. Phase identification was performed by matching observed reflections to the Powder

**Table 1**  
Nominal compositions of the studied sealants.

Composition	Nominal molar fraction, %				
	BaO	CaO	$\text{Al}_2\text{O}_3$	$\text{SiO}_2$	$\text{B}_2\text{O}_3$
Si52B09	17	17	5	52	9
Si55B06	17	17	5	55	6
Si58B03	17	17	5	58	3
Si61B00	17	17	5	61	0

Diffraction File (PDF) database using Match! software. Crystalline phase quantification and assessment of crystallinity were achieved through Rietveld refinement.

The crystallization behavior of the sealants following 100 h of exposure to simulated operating temperatures was further investigated using scanning electron microscopy (SEM). A Supra 50 VP microscope (Carl Zeiss, Germany) was used to acquire images of polished sample surfaces without chemical etching. The deliberate omission of chemical etching ensured that the elemental composition of localized crystalline structures remained unaltered for subsequent analysis using energy-dispersive X-ray spectroscopy (EDS) with an INCA system (Oxford Instruments, UK).

The evolution of the sealants' phase composition during prolonged exposure to simulated operating temperatures was also investigated using *in-situ* high-temperature Raman spectroscopy. Raman spectra were collected using a home-made apparatus described in our previous works [37,38]. This setup uses a semiconductor laser with a wavelength of 532 nm as excitation source, an optical system and liquid nitrogen-cooled CCD detector (Princeton Instruments, USA) give opportunity to collect the scattered radiation, and a high-temperature furnace where the samples were held controls working temperature. Spectra were collected from pressed sealant powders at room temperature, at elevated temperature prior to simulated sealing, immediately after simulated sealing, and during isothermal holds at the operating temperature after various exposure durations. In order to correct the results on thermal radiation emitted by the heated sample, background spectra were collected with

the laser source blocked by aperture shutter and subsequently subtracted from the experimental data (typical time periods for spectra collection with open and closed laser were 1 s each as higher time periods lead to dramatic temperature changes, thermal radiation spectra are strongly influenced by temperature). Additionally, spectral intensities were normalized in order to account for the temperature-dependent Bose-Einstein phonon occupation numbers.

Differential scanning calorimetry (DSC) was employed to determine the glass transition temperature ( $T_g$ ) and crystallization temperatures ( $T_p$ ) of the sealants. Measurements were performed using a STA 449 F1 Jupiter thermal analysis system (NETZSCH, Germany). Samples were analyzed in platinum crucibles under an argon atmosphere with a gas flow rate of 30 mL/min. The temperature program consisted of heating from 30 °C to 950 °C at a rate of 20 °C/min.

### 3. Results

#### 3.1. X-ray diffraction (isothermal aging)

Fig. 1 shows XRD patterns for as-cast and heat-treated sealants. To minimize geometric effects, all samples were ground after casting or heat treatment. As-cast sealants exhibited broad, diffuse halos at similar  $2\theta$  values, indicating amorphous character. The absence of distinct crystalline peaks suggests complete melting and rapid quenching, effectively preventing crystallization.

The sealants remained amorphous after heat treatment at 750 °C.

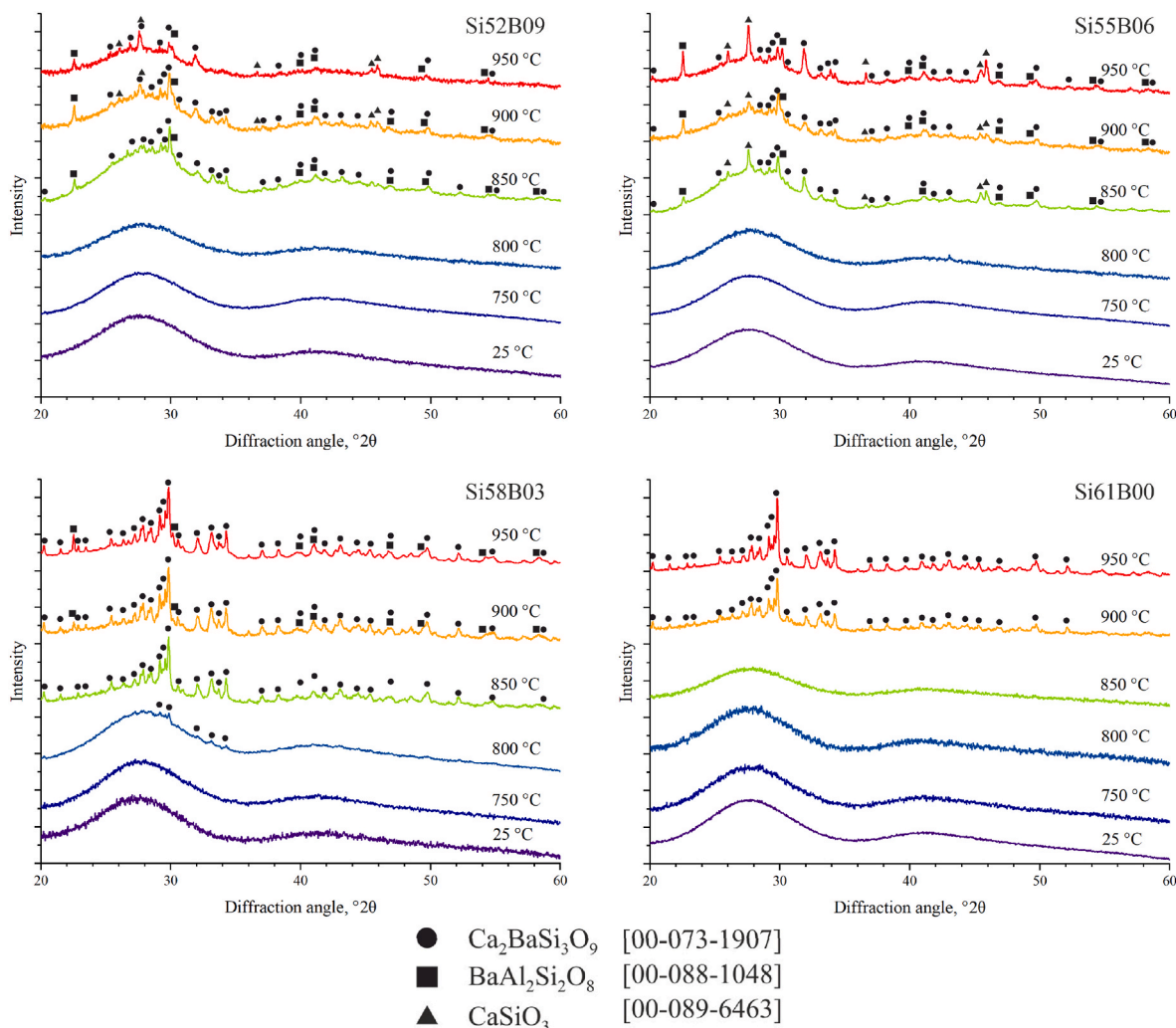


Fig. 1. X-ray diffraction patterns of the cast and heat-treated sealants.

However, minor crystallization began to emerge at 800 °C, with early signs of crystallinity particularly evident in the XRD patterns of Si55B06 and Si58B03. Upon heating to 850 °C and holding for 1.5 h, significant crystallization occurred in the Si52B09–Si58B03 sealants, as shown in Fig. 1. Further increases in heat-treatment temperature also induced partial crystallization in the Si61B00 sealant. The primary crystalline phases identified in the studied sealants include  $\text{Ca}_2\text{BaSi}_3\text{O}_9$  (walstromite structure; ICDD 00-073-1907),  $\text{BaAl}_2\text{Si}_2\text{O}_8$  (hexacelsian structure; ICDD 00-088-1048), and  $\text{CaSiO}_3$  (pseudowollastonite structure; ICDD 00-089-6463). Fig. 2 presents the fraction of retained amorphous phase and the percentage of crystalline phases after heat treatment in 850–950 °C range, as determined by Rietveld refinement. Third-order polynomial was used for background fitting to ensure accurate calculation of amorphous phase content.

In order to conveniently present fractions of crystalline phases in samples with high content of amorphous phase, the following procedure for graphical presentation is used. Black bars show fractions of amorphous phase in the entire sample. The colored bars show percentage of the specific crystalline phases in the crystalline part of the sample. That is fraction, of crystalline phases is normalized over total crystallinity of the sample.

Fig. 2 shows that the amorphous phase fraction remains above 50 vol % across the studied temperature range after heat treatment. XRD analysis identified walstromite ( $\text{Ca}_2\text{BaSi}_3\text{O}_9$ ) as the dominant crystalline phase in all samples and at all treatment temperatures, typically exceeding 90 vol %. An exception was the Si55B06 composition, in which a significant quantity of pseudowollastonite ( $\text{CaSiO}_3$ ) crystallized. Notably, major quantity of  $\text{CaSiO}_3$  was only observed in the Si55B06 composition; no XRD reflections corresponding to this phase were detected in Si58B03 and Si61B00, and only minor quantity was

observed in Si52B09. Hexacelsian  $\text{BaAl}_2\text{Si}_2\text{O}_8$  was consistently present as a minor phase in all studied compositions and at all temperatures.

### 3.2. Hot stage microscopy

For SOFC sealing sealants typically undergo a brief (up to a few hours) high-temperature treatment, followed by prolonged exposure to the operating temperature, which is approximately 100 °C lower. Data from constant-temperature heat treatments may not accurately predict the extent of crystallization and the dominant crystalline phases under sealing and operating conditions. Therefore, we used hot-stage microscopy to estimate the sealing and operating temperatures of the studied sealants, enabling subsequent heat treatments that simulated their use in SOFCs.

Table 2 summarizes our findings on the effect of  $\text{SiO}_2$  and  $\text{B}_2\text{O}_3$  content on high-temperature behavior of the studied sealants. The key temperatures of the sealants increased significantly and monotonically with increasing  $\text{SiO}_2$  content. For example, the ball formation point

**Table 2**  
Sintering, softening, ball, half-ball and flow temperatures of the studied sealants determined by means of hot-stage microscopy.

Temperature, °C	Composition			
	Si52B09	Si55B06	Si58B03	Si61B00
<b>Sintering</b>	755 ± 3	770 ± 3	796 ± 3	825 ± 3
<b>Softening</b>	844 ± 3	869 ± 3	905 ± 3	945 ± 3
<b>Ball</b>	865 ± 3	910 ± 3	943 ± 3	975 ± 3
<b>Half-ball</b>	944 ± 3	1014 ± 3	1088 ± 3	>1100
<b>Flow</b>	971 ± 3	1047 ± 3	1098 ± 3	>1100

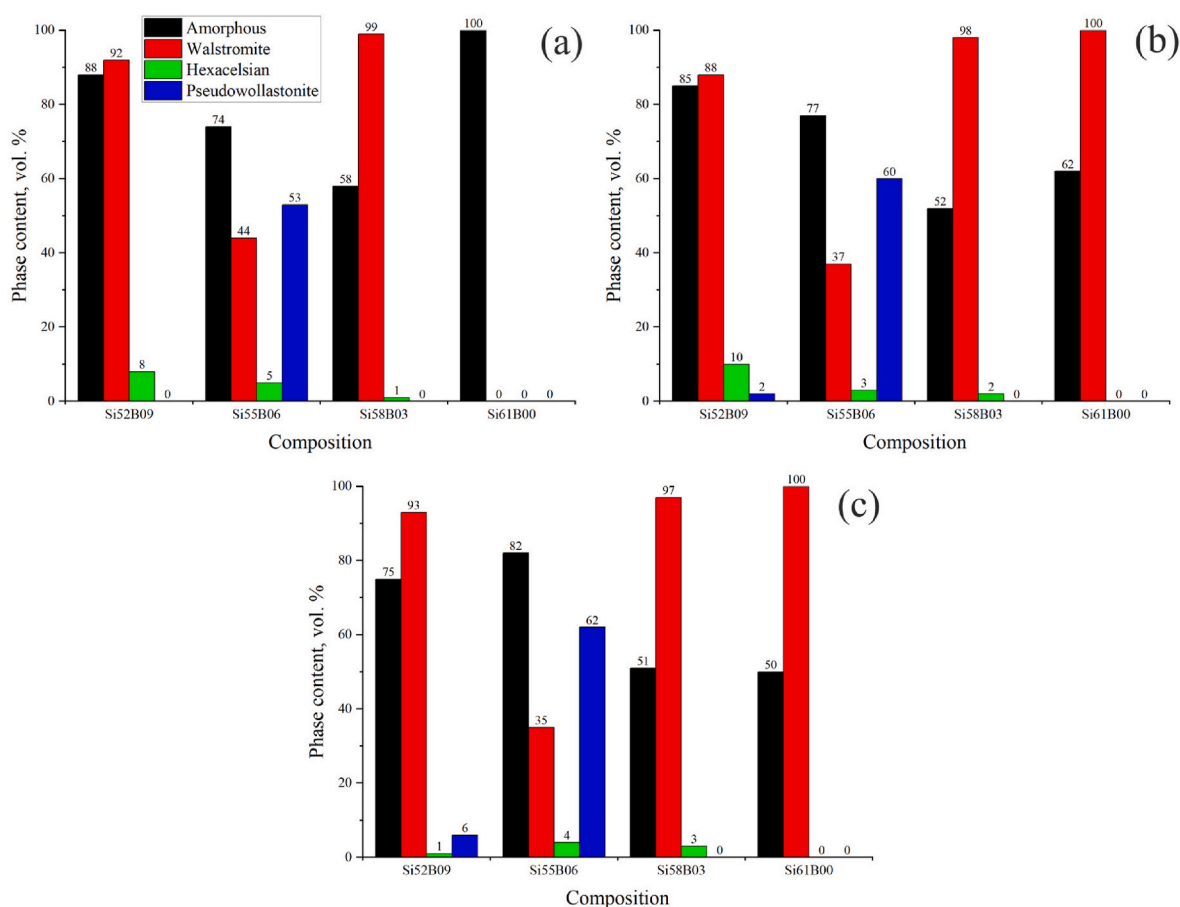


**Fig. 2.** Fraction of amorphous phase and content of crystalline phases in the sealants after heat treatment at: (a) 850 °C, (b) 900 °C, (c) 950 °C.

increased by 110 °C when 9 mol% of B<sub>2</sub>O<sub>3</sub> were replaced with SiO<sub>2</sub>. Other key temperatures were less sensitive to the sealant composition. The half-ball and melting temperatures for the Si61B00 composition were above the tested temperature range. For determining suitable sealing and operating temperatures, the ball formation temperature provides a reasonable approximation of the sealing temperature. The operating temperature is typically about 100 °C below the sealing temperature. For optimal seal quality and lifetime, the operating temperature should be above the glass transition temperature but below the softening temperature. The latter condition minimizes the risk of the seal being displaced by gas pressure.

### 3.3. Differential scanning calorimetry

Differential scanning calorimetry was employed to characterize the thermal behavior of the sealants, specifically to determine their glass transition and crystallization temperatures. Representative DSC curves for each sealant are shown in Fig. 3. All samples exhibited a well-defined glass transition, with the  $T_g$  increasing with increasing SiO<sub>2</sub> content. The observed  $T_g$  values were 695 °C, 710 °C, 730 °C, and 765 °C for the Si52B09, Si55B06, Si58B03, and Si61B00 compositions, respectively. These  $T_g$  values were significantly lower than the estimated operating temperatures.

The crystallization (devitrification) signals in the high-temperature region of the DSC curves were of low intensity, making them difficult to identify and accurately determine their positions. Weak crystallization peaks were observed at 900–920 °C in the DSC curves for the Si52B09, Si58B03, and Si61B00 samples. A poorly defined peak was also detected at approximately 820 °C in the Si52B09 curve. These low-intensity crystallization peaks observed in the DSC data appear to be inconsistent with the XRD data (Figs. 1 and 2). This apparent discrepancy can be attributed to a low crystallization rate, which limits the formation of the crystalline phase during the relatively short DSC measurement.

### 3.4. X-ray diffraction (sealing and operating)

Fig. 4 shows XRD patterns of the sealants following a 1.5-h sealing process at their respective ball formation temperatures and subsequent holding at the expected operating temperature (100 °C lower) for 1 h and 100 h. The specific sealing and operating temperatures for each sealant are indicated in the figure subplots. As expected, all sealants exhibited some degree of crystallization after prolonged exposure to the operating temperature. Notably, the most extensive crystallization occurred in the Si52B09 and Si55B06 compositions, which had the

lowest initial degree of crystallization and were held at the lowest operating temperatures. Indeed, the presence of any remaining amorphous phase in Si52B09 and Si55B06 is difficult to ascertain from the XRD patterns without detailed Rietveld refinement. In contrast, the sealants with higher silica content displayed a greater initial degree of crystallization but significantly less pronounced continued crystallization upon exposure to the operating temperatures.

The obtained XRD patterns are complex, particularly for the Si52B09 and Si55B06 compositions, which contain numerous crystalline phases. Identified phases include walstromite (Ca<sub>2</sub>BaSi<sub>3</sub>O<sub>9</sub>), hexacelsian (BaAl<sub>2</sub>Si<sub>2</sub>O<sub>8</sub>), and pseudowollastonite (CaSiO<sub>3</sub>), consistent with phases detected in earlier isothermal hold tests (Figs. 1 and 2). Furthermore, high-intensity peaks corresponding to Itsiite (Ba<sub>2</sub>Ca(BSi<sub>2</sub>O<sub>7</sub>)<sub>2</sub>) were identified in Si52B09 and Si55B06. Rietveld refinement was used to quantify the content of the remaining amorphous phase and the fractions of each crystalline phase. The results of this analysis are presented in Fig. 5. For graphical presentation we used the same normalization procedure as the one used for Fig. 2.

After the 100-h exposure, the Si52B09 sealant contained a minor amount of amorphous phase, approximately 18 %, a significant decrease from its nearly fully amorphous structure after the 1-h exposure. The dominant crystalline phase in this sample was itsiite (Ba<sub>2</sub>Ca(BSi<sub>2</sub>O<sub>7</sub>)<sub>2</sub>), with a volumetric fraction of about 70 %.

The Si55B06 sample exhibited less pronounced crystallization upon prolonged exposure. Here, the amorphous phase content decreased from 67 % to 25 %. A notable change was observed in the crystalline phase composition of the Si55B06 sealant during the 100-h exposure. After the 1-h exposure, walstromite and pseudowollastonite were the major phases, while Itsiite and hexacelsian were present in amounts less than 10 %. However, after the 100-h exposure, the phase composition shifted significantly due to further crystallization and, potentially, recrystallization. Itsiite became the dominant crystalline phase, with the walstromite and pseudowollastonite content dropping to approximately 10 %.

The Si58B03 and Si61B00 compositions displayed a much simpler crystallization behavior. In both compositions, walstromite was the major phase. Si58B03 also contained a minor amount of hexacelsian. These sealants showed very slight crystallization during the 100-h exposure, with the majority of crystallization occurring during the sealing stage.

### 3.5. Scanning electron microscopy

The evolution of the crystalline structure is further illustrated by the SEM images in Fig. 6.

The most pronounced changes in microstructure upon prolonged exposure to the operating temperature were observed in the Si52B09 and Si55B06 samples. The microstructure of Si52B09 after 1 h showed only a few crystallites, up to 20–30 μm in size. After the 100-h exposure, a complex crystalline structure developed in Si52B09, exhibiting at least three distinct regions with varying contrast in the SEM image.

In agreement with the XRD data, Si55B06 showed a greater degree of visible crystallization after 1 h. Large, needle-shaped crystals, likely corresponding to pseudowollastonite (CaSiO<sub>3</sub>), were observed in the microstructure after 1 h. These crystals were not detected in the other compositions. After 100 h, numerous elongated crystals formed in Si55B06. Furthermore, the “background” gray structure was not uniform; at least two regions differing in SEM contrast were observed.

The SEM images of the Si58B03 and Si61B00 sealants showed much less pronounced visible structural changes. These compositions, after both the 1-h and 100-h exposures, appeared as a rather homogeneous gray phase in SEM contrast, with some needle-shaped dark crystals interspersed throughout the volume. The fraction of these crystals did not change significantly with increased exposure time. Again, these observations qualitatively agree with the XRD data.

EDS was employed to determine the chemical composition of the

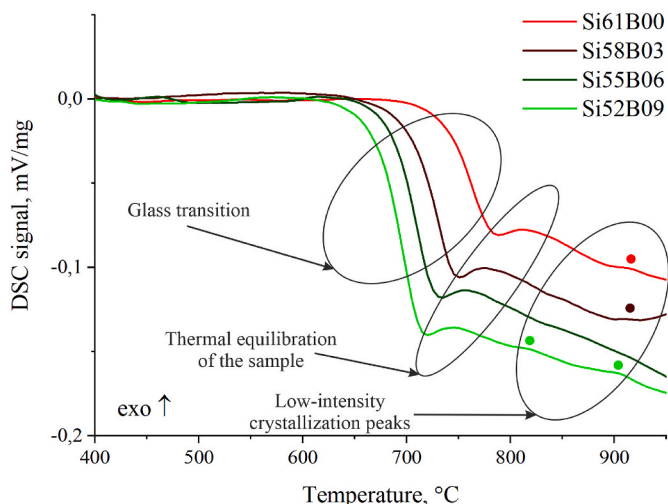


Fig. 3. DSC curves of the sealant powders.

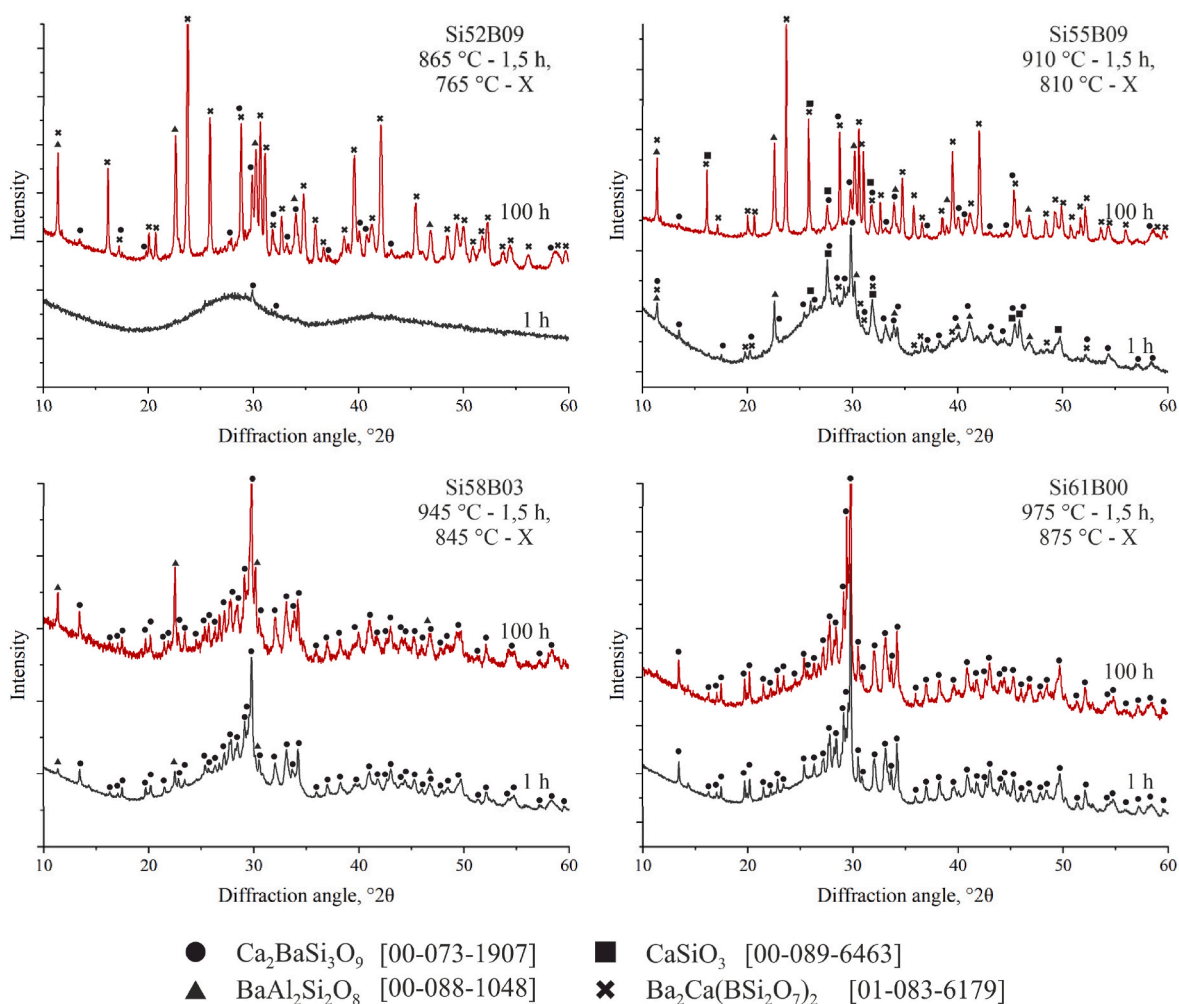


Fig. 4. XRD patterns of the sealants after 1-h and 100-h exposure to operating temperature following a simulated sealing process.

crystalline phases identified in the SEM images. Fig. 7 highlights the microstructural features analyzed, including regions with distinct SEM contrast variations and crystalline formations of differing morphologies. Spectra were collected from homogeneous areas where possible to ensure representative compositional data.

Table 3 summarizes the EDS results, showing the atomic percentages of Ba, Ca, Si, and Al. Oxygen content is omitted for simplicity, while boron is undetectable by EDS. It is important to note that the reported values may slightly deviate from the true composition of the analyzed microstructural features. This uncertainty arises because the spectra were acquired from a finite area rather than a single point, meaning the signal could include contributions from the surrounding material.

The most striking trend in Table 3 is the distinct compositional contrast between the dark and light crystalline phases. The dark formations exhibit low barium and aluminum content but are enriched in calcium, while maintaining near-constant silicon levels. This suggests they consist primarily of calcium silicate or a low-barium mixed silicate such as walstromite ( $\text{Ca}_2\text{BaSi}_3\text{O}_9$ ). In contrast, the lighter regions likely contain hexacelsian ( $\text{BaAl}_2\text{Si}_2\text{O}_8$ ) or itsite ( $\text{Ba}_2\text{Ca}(\text{BSi}_2\text{O}_7)_2$ ), consistent with their higher Ba and Al signals.

### 3.6. Raman spectroscopy

Fig. 8 presents the results of *in-situ* Raman spectroscopy performed on the sealants following the sealing process and during exposure to the operating temperature for 100 h. Spectra were collected at fixed intervals of 20 h. The spectra for Si52B09 exhibit a broad spectral line in

the approximate range of  $850\text{--}1100\text{ cm}^{-1}$ . This region is characteristic of vibrations associated with silicate tetrahedra having varying numbers of bridging oxygen (BO) atoms. Higher Raman shifts are generally correlated with a greater number of BOs. The following peak positions are commonly reported: 4 BOs –  $1200\text{ cm}^{-1}$ , 3 BOs –  $1050\text{--}1100\text{ cm}^{-1}$ , 2 BOs –  $950\text{--}1000\text{ cm}^{-1}$ , 1 BOs –  $900\text{ cm}^{-1}$ , and 0 BOs –  $850\text{ cm}^{-1}$  [39,40]. The absence of a peak at  $1200\text{ cm}^{-1}$  in the Si52B09 spectra indicates that silicate tetrahedra with 4 BOs are not present, consistent with the sealant's chemical composition. The broad spectral line observed between  $850$  and  $1100\text{ cm}^{-1}$  is analyzed in further detail in Fig. 9. The lower Raman shift range ( $100\text{--}600\text{ cm}^{-1}$ ) provides limited information on the Si52B09 sealant because of the lack of identifiable spectral lines. Notably, the Si52B09 spectra exhibit no significant changes during the 100-h exposure to the operating temperature.

The Raman spectra of Si55B06 sealant differ significantly from those of Si52B09. An intense peak emerges at approximately  $980\text{ cm}^{-1}$  and becomes more pronounced with increasing exposure time. The lower Raman shift region ( $200\text{--}650\text{ cm}^{-1}$ ) also exhibits several peaks, the most intense of which are located at  $642$ ,  $570$ , and  $500\text{ cm}^{-1}$ . Increased exposure time leads to changes in the relative intensities of the peaks within this lower Raman shift region. Specifically, the peak at  $642\text{ cm}^{-1}$  shift becomes more prominent, while the peak at  $600\text{--}610\text{ cm}^{-1}$  nearly disappears.

Consistent with the XRD data, which indicated similar degrees of crystallization and  $\text{BaCa}_2\text{Si}_3\text{O}_9$  as the dominant crystalline phase in both compositions, the Raman spectra for Si58B03 and Si61B00 are similar to each other. The peak at approximately  $980\text{ cm}^{-1}$  shift is more intense

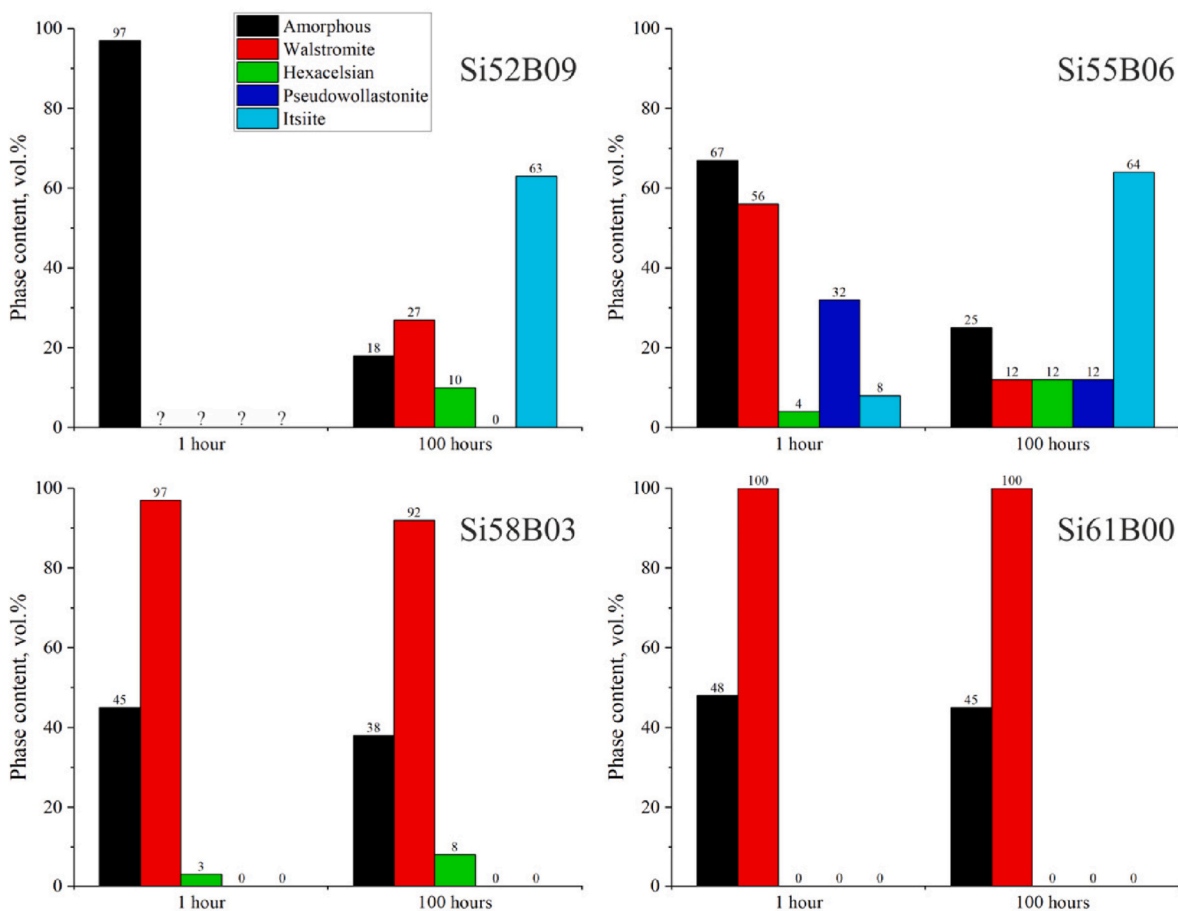


Fig. 5. Fraction of amorphous phase and content of crystalline phases in the sealants after sealing and exposure to predicted operating temperatures for 1-h and 100-h periods.

than that observed in the Si55B06 spectra. The lower shift region also exhibits more pronounced peaks, showing minimal change with increased exposure time. A detailed description of the peak positions is provided in Fig. 9.

The lower part of Fig. 9 illustrates the decomposition of the broad line observed in the Si52B09 spectra, spanning the range of 850–1100  $\text{cm}^{-1}$ . This signal was decomposed into two Gaussian components, with maxima located at 930  $\text{cm}^{-1}$  and 1030  $\text{cm}^{-1}$  respectively. These values approximate the Si–O vibrational modes in silicate tetrahedra possessing two and three BOs, respectively [39,40]. However, the observed maxima are shifted towards lower Raman shifts compared to the reported values. The relative areas of these decomposed peaks are in the ratio of 0.3:1, which is in qualitative agreement with the chemical composition of Si52B09. These peaks are also observed in the Raman spectra of the other sealants (indicated by vertical lines).

The Raman spectra of the Si55B06–Si61B00 sealants exhibit clearly defined peaks, although these peaks are least pronounced in the Si55B06 spectrum, particularly in the lower Raman shift region. The observed peaks can be reliably attributed to the crystalline phases identified previously using XRD, based on literature data:  $\text{CaSiO}_3$  and  $\text{Ca}_2\text{BaSi}_3\text{O}_9$  [41], hexacelsian  $\text{BaAl}_2\text{Si}_2\text{O}_8$  [42],  $\text{Ba}_2\text{Ca}(\text{BSi}_2\text{O}_7)$  (RRUFF database, [43]). The most intense peaks often corresponded to multiple phases due to the presence of similar structural elements in different crystalline phases.

#### 4. Discussion

X-ray diffraction analysis indicates that the degree and extent of crystallization resulting from isothermal aging do not accurately reflect

the crystallization behavior under simulated operating conditions. These conditions are characterized by a complex thermal profile, including a short, high-temperature exposure during sealing (typically 100 °C above the operating temperature) followed by extended aging at the operating temperature. The contrast is evident upon comparing Figs. 1 and 2 (isothermal aging) with Figs. 3 and 4 (simulated operating conditions).

Following isothermal aging, XRD patterns predominantly reveal the presence of walstromite ( $\text{Ca}_2\text{BaSi}_3\text{O}_9$ ) as the dominant phase, along with some hexacelsian ( $\text{BaAl}_2\text{Si}_2\text{O}_8$ ) and pseudowollastonite ( $\text{CaSiO}_3$ ). Pseudowollastonite was only detected in significant quantity in the Si55B06 composition; although minor amount of pseudowollastonite was also observed in Si52B09. In contrast to previous reports on barium aluminosilicate sealants [23,28,32,44], we detected no monoclinic  $\text{BaAl}_2\text{Si}_2\text{O}_8$  phase, which is typically formed via transformation of metastable hexacelsian at elevated temperatures [29]. Furthermore, no boron-containing crystalline phases were observed. This suggests that boron oxide remained within the glassy phase.

A notable result of the isothermal aging experiment is the unique appearance of large quantities of pseudowollastonite ( $\text{CaSiO}_3$ ) phase in the Si55B06 composition. While pseudowollastonite formation is typically reported in calcium aluminosilicate systems, [45], our research observed it in a barium-calcium aluminosilicate system. To ensure that the presence of this phase did not arise from sample contamination, incomplete batch melting, or insufficient quenching, multiple preparations of the Si55B06 sealant were performed. The  $\text{CaSiO}_3$  phase was consistently confirmed across all attempts. However, the underlying reasons for its formation in this specific composition remain unclear within the scope of the present research.

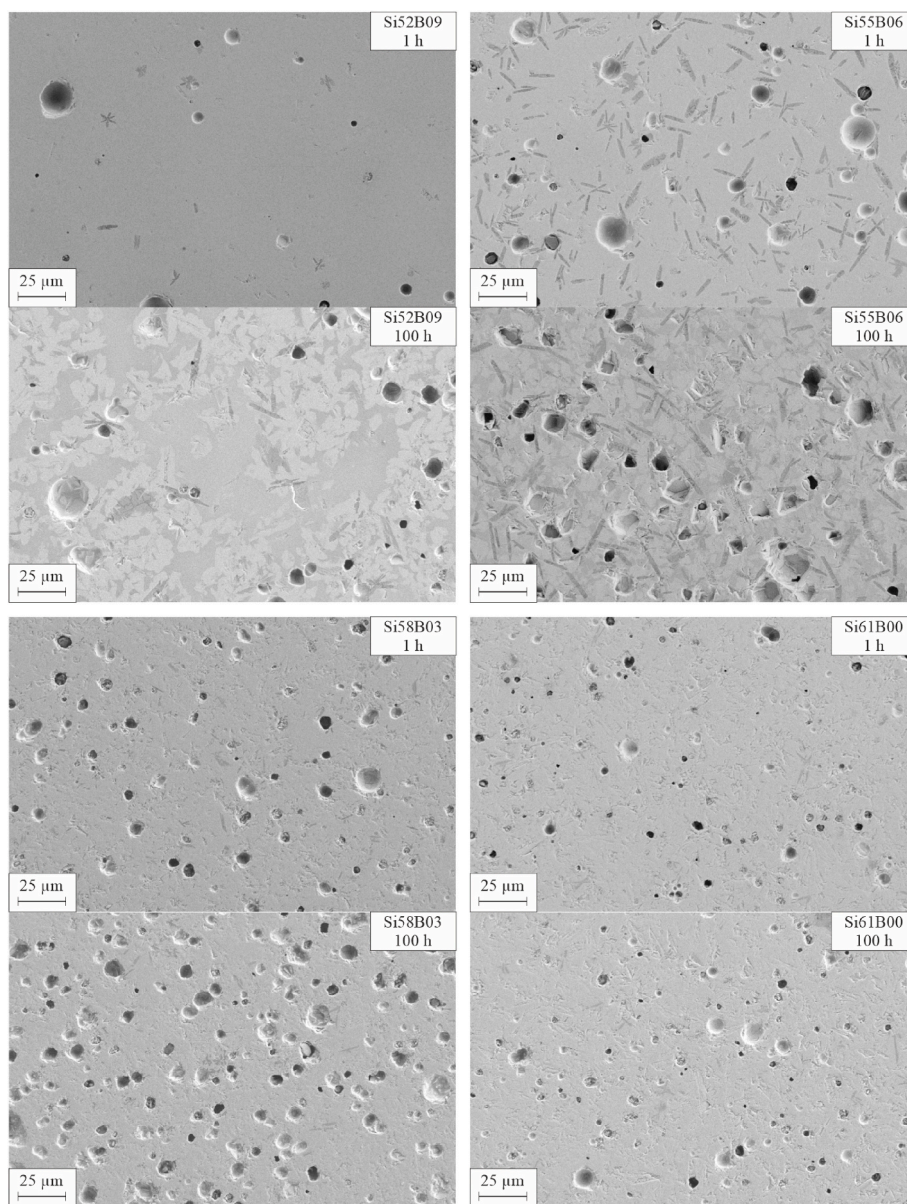


Fig. 6. SEM images of the studied sealants after sealing and aging for 1 h and 100 h.

In contrast to the results obtained after isothermal aging, XRD analysis of the sealants following heat treatment under simulated operating conditions revealed a different crystallization pattern. These simulated operating conditions were defined based on ball formation temperatures determined by HSM and glass-transition temperatures obtained from DSC. The primary distinction was the crystallization of a phase unobserved after isothermal aging:  $\text{Ba}_2\text{Ca}(\text{BSi}_2\text{O}_7)$  (itsiite) [43]. The appearance of itsiite phase was exclusive to Si52B09 and Si55B06, potentially due to two contributing factors. Firstly, these compositions possess a higher boron content. Secondly, their operating temperatures (765 °C and 810 °C, respectively) are relatively low, below the temperatures at which significant crystallization occurred during isothermal aging. However, the higher boron content is unlikely to be the sole determinant, as itsiite was absent during isothermal aging of these same compositions. This suggests that itsiite crystallization is favored within temperature range of approximately 750–800 °C. Unfortunately, this hypothesis is difficult to validate using DSC data, as the crystallization peaks were weak across all samples.

The Si52B09 and Si55B06 sealants crystallized more readily at their operating temperatures than Si58B03 and Si61B00. This is evidenced by

the significant reduction in amorphous phase content, dropping from 97 % to 17 % in Si52B09 and from 67 % to 25 % in Si55B06. The high crystallization rate observed in these B2O3-rich compositions is unusual, given that boron oxide is generally understood to act as a crystallization inhibitor in silicate glasses [46]. Considering that itsiite is the dominant crystalline phase in these compositions, the high crystallization rate observed in Si52B09 and Si55B06 sealants is likely driven primarily by its rapid crystallization. The lower overall crystallization in Si55B06 is probably due to its reduced boron content, which limits the potential for itsiite formation. It can be inferred that prolonged exposure of Si58B03 to temperatures within the 750–800 °C range would likely result in significant itsiite crystallization.

Following sealing and a 1-h exposure to the operating temperature, the Si55B06 sealant predominantly contained walstromite, with a significant proportion (approximately 30 %) of pseudowollastonite. This observation aligns with the findings from isothermal aging experiments. However, after 100 h at the operating temperature, the fractions of these phases substantially decreased, and itsiite emerged as the dominant phase, exceeding 60 %. Unlike Si52B09, where itsiite crystallized directly from a nearly fully amorphous matrix after sealing, itsiite in

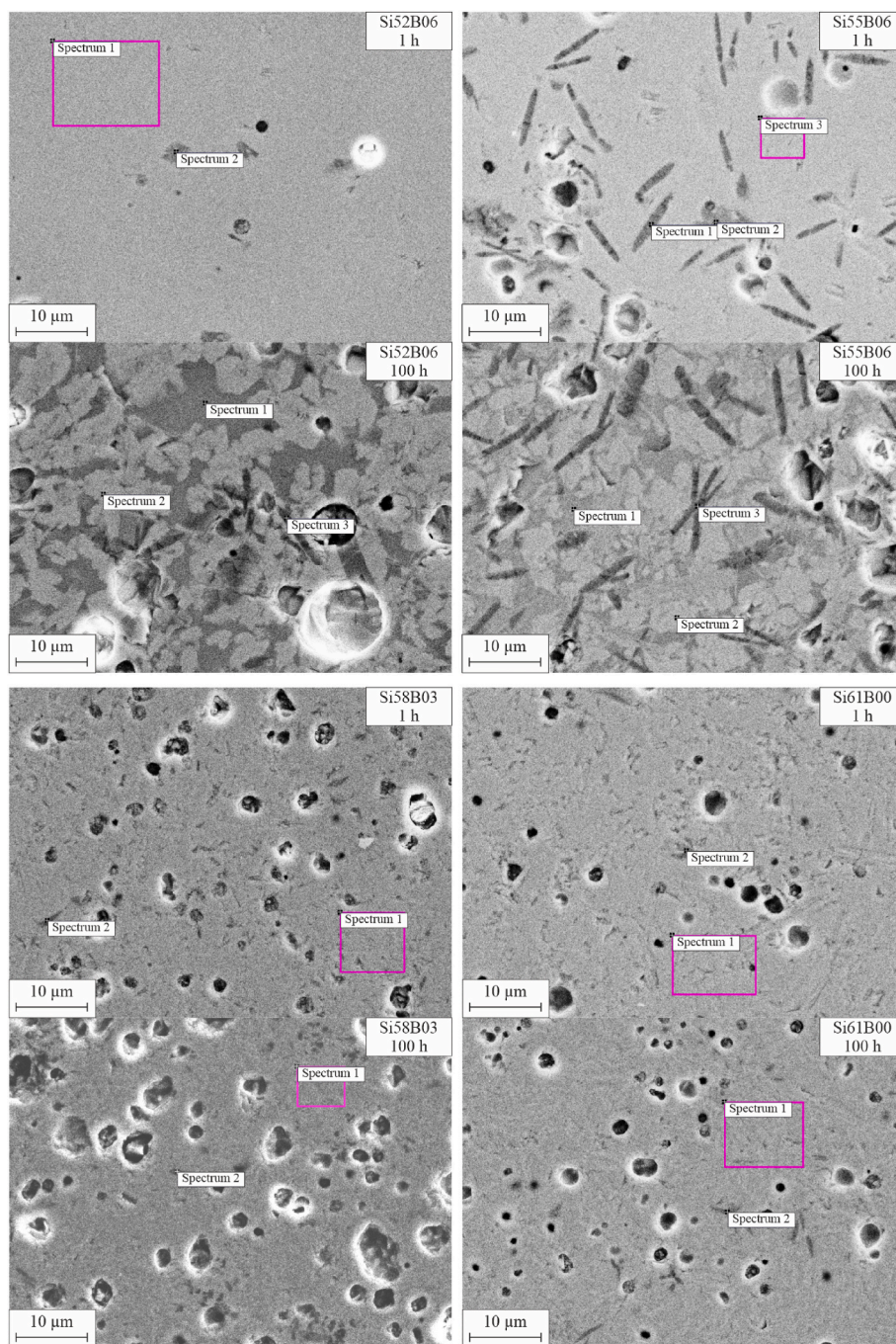


**Fig. 7.** Points at which EDS spectra were taken on the samples. Pink rectangles indicate the spectra collected over area. (For interpretation of the references to color in this figure legend, the reader is referred to the Web version of this article.)

Si55B06 developed through the recrystallization of walstromite and pseudowollastonite crystals, as well as the amorphous matrix. This shift in crystalline composition cannot be attributed to misinterpretation of the XRD patterns, as itsite exhibits distinct and intense X-ray reflections that do not overlap with those of walstromite and pseudowollastonite. While the precise quantitative determination of phase fractions may be subject to some uncertainty, the qualitative assessment of itsite's dominance is considered reliable.

The impact of substantial itsite formation on the suitability of these sealants for SOFC applications is currently uncertain, primarily due to the limited availability of thermal expansion data for this phase. We attempted to measure CTE of itsite. For this purpose we tried to synthesize a single-phase itsite sample through heat treatment of a

stoichiometric glass composition, but the presence of secondary phases precluded us from obtaining reliable dilatometric measurements. Despite the lack of definitive thermal property data for itsite, it can be concluded that the rapid crystallization observed in Si52B09 and Si55B06 likely compromises their performance in SOFC systems, at least at the simulated operating temperatures investigated in this study.

The crystallization behavior of Si58B03 and Si61B00 contrasted significantly with that of Si52B09 and Si55B06. Following the sealing process, the amorphous phase fraction in these sealants was already slightly below 50%. However, unlike Si52B09 and Si55B06, subsequent crystallization occurred at a considerably slower rate. Specifically, after a 100-h exposure, the amorphous phase fractions were approximately 38% and 45% in Si58B03 and Si61B00, respectively.

**Table 3**

Elemental compositions of microstructural features in the heat-treated sealants (oxygen excluded, unnormalized).

Sample	Spectrum collection region	Element content, at. %			
		Ba	Ca	Si	Al
Si52B09 1 h	1. Featureless gray area	6	10	17	3
	2. Dark crystalline inclusion	2	20	17	3
Si52B09 100 h	1. Gray region	4	8	18	4
	2. Light-colored region	8	7	17	3
	3. Dark needle-shaped crystal	2	18	17	1
Si55B06 1 h	1. Dark needle-shaped crystal	2	22	18	1
	2. Dark crystalline inclusion	1	22	18	2
	3. Featureless gray area	6	10	19	3
Si55B06 100 h	1. Gray region	6	3	23	4
	2. Light-colored region	9	6	19	4
	3. Dark needle-shaped crystal	0	22	17	1
Si58B03 1 h	1. Gray area, small crystals.	7	10	19	3
	2. Dark crystalline inclusion	2	19	17	1
Si58B03 100 h	1. Gray area, small crystals	6	8	20	3
	2. Dark crystalline inclusion	2	19	18	1
Si61B00 1 h	1. Gray area, small crystals	7	8	22	4
	2. Dark crystalline inclusion	3	15	21	2
Si61B00 100 h	1. Gray area, small crystals	6	9	20	3
	2. Dark crystalline inclusion	2	18	16	2

Furthermore, the phase composition of the crystalline phases in these sealants exhibited minimal change upon prolonged exposure. Walstromite remained the dominant crystalline phase in both compositions, with minor quantities of hexacelsian observed in Si58B03.

The slow crystallization rate observed at the operating temperature makes the Si58B03 and Si61B00 compositions promising candidates for SOFC applications. This potential is further supported by the favorable thermomechanical compatibility of the original amorphous sealant, as

previously reported [36] and by the suitable CTEs of the crystalline phases formed in these compositions with other components of SOFC systems. Specifically, CTE of hexacelsian  $\text{BaAl}_2\text{Si}_2\text{O}_8$  has been reported in the context of SOFC applications to be in the range of  $9\text{--}13 \times 10^{-6} \text{ K}^{-1}$  [25]. We determined the CTE of walstromite using the same method we previously employed for itsite, obtaining a value of  $10.8 \pm 0.3 \times 10^{-6} \text{ K}^{-1}$  in the  $100\text{--}600 \text{ }^\circ\text{C}$  range.

SEM combined with EDS provides qualitative support for the XRD results. Following a 1-h exposure to the operating temperature, Si52B09 and Si55B06 sealants exhibit a homogeneous gray matrix with minor (Si52B09) to moderate (Si55B06) amounts of dark crystalline formations. In Si52B09, these crystalline formations are generally below  $3 \mu\text{m}$  in size and possess relatively uniform dimensions. By contrast, Si55B06 displays predominantly needle-like crystals, reaching lengths of up to  $10 \mu\text{m}$ , alongside smaller dark crystalline areas similar to those observed in Si52B09. Quantitative analysis of EDS spectra acquired from all three types of crystalline regions revealed no significant compositional differences. Notably, these crystalline regions are barium-deficient compared to the surrounding amorphous matrix. Given the finite sampling area of EDS, the detected barium signal may originate from the surrounding matrix rather than from within the crystals themselves. By correlating the compositional data from Table 2 with the phase composition determined by XRD (Fig. 5), we can reasonably conclude that these crystals correspond to walstromite (in both sealant compositions) and pseudowollastonite (in Si55B06).

After a 1-h exposure, microstructures of Si58B03 and Si61B00 exhibit a gray amorphous matrix interspersed with darker crystals. These dark crystalline formations, like those in the previous compositions, are barium-deficient. Combining this observation with the XRD results, we can confidently identify these formations as walstromite crystals. By comparing the morphology of walstromite crystals in

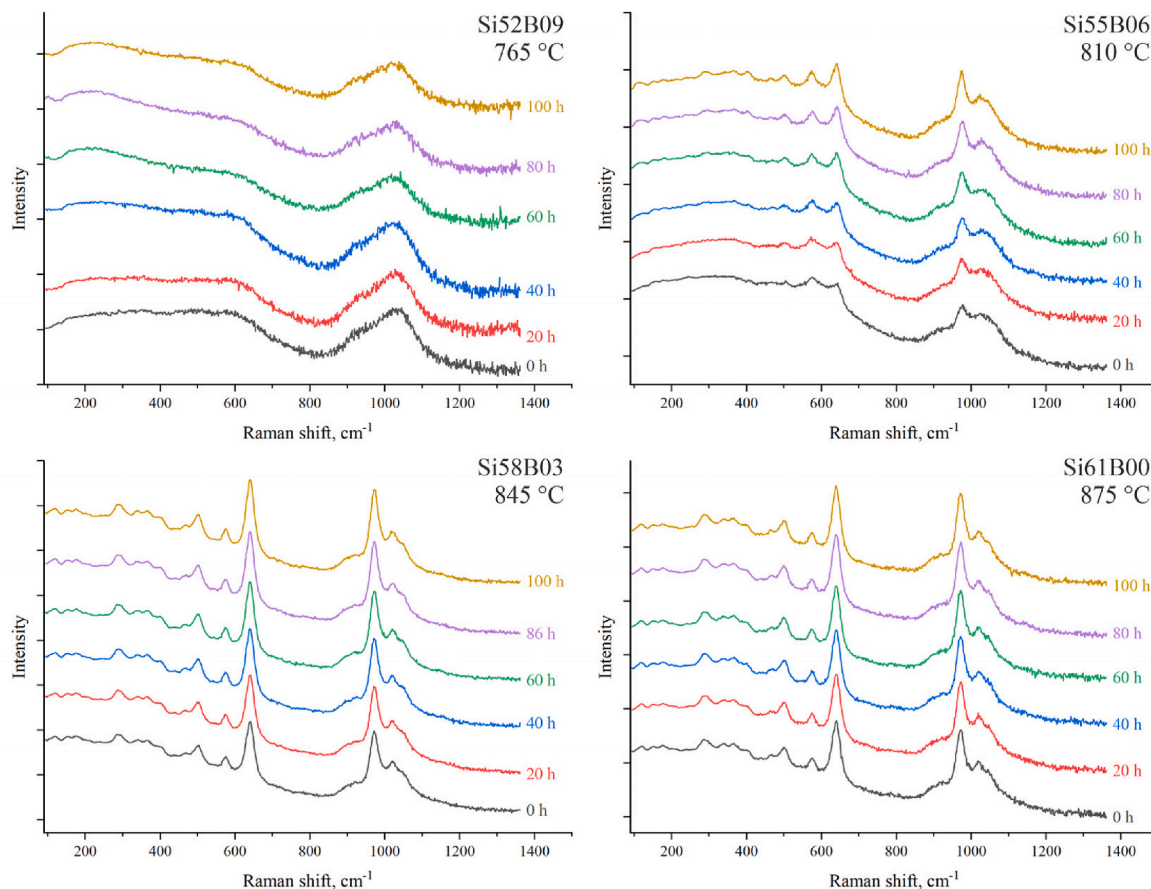


**Fig. 8.** *In-situ* Raman spectra of the sealants after sealing and exposure to operating temperatures (0–100 h).

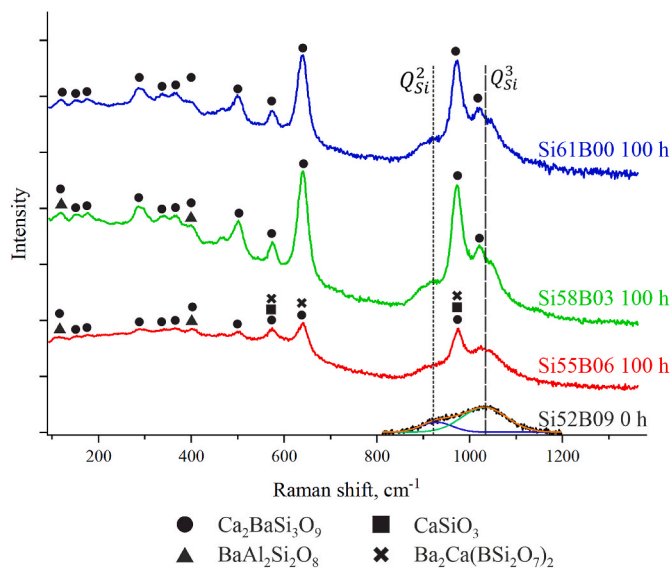


Fig. 9. Selected Raman spectra of the sealants.

Si58B03 and Si61B00 with the two distinct types of crystals present in Si55B06, we can infer that the elongated crystals displaying a darker SEM contrast in Si55B06 are CaSiO<sub>3</sub> (pseudowollastonite) crystals.

SEM images of Si58B03 and Si61B00 following a 100-h exposure reveal no discernible differences compared to images of the 1-h exposed sealants. There are no new microstructural features or significant changes in the proportion of existing features. This consistency aligns well with the XRD data obtained for these sealants. From a long-term phase stability perspective, Si58B03 and Si61B00 appear to be the most promising compositions among those studied.

In contrast to Si58B03 and Si61B00, the Si52B09 and Si55B06 sealants exhibit a significantly more complex microstructure after a 100-h exposure. The dark-contrast, elongated crystals previously identified as CaSiO<sub>3</sub> (pseudowollastonite) remain visible, with their proportion being notably higher in Si55B06, though visually the fraction appears to have decreased compared to the 1-h exposure. In the previously uniform amorphous matrix, a new crystalline phase with a light SEM contrast has emerged. This phase is enriched in barium compared to both the initial amorphous matrix (as seen in the 1-h SEM images) and the darker, presumably amorphous areas present after the 100-h exposure (Spectrum 1 for both Si52B09 and Si55B06). The high proportion of this barium-rich phase, in conjunction with the XRD data, strongly indicates that it is itsite (Ba<sub>2</sub>Ca(BSi<sub>2</sub>O<sub>7</sub>)<sub>2</sub>). The itsite crystals form large, contiguous regions, seemingly devoid of any residual amorphous phase. This rapid formation of a new phase after only 100 h of operation raises concerns about the long-term phase stability and thermomechanical compatibility of Si52B09 and Si55B06 sealants under operating conditions, despite the favorable CTEs of the initial sealant compositions [36]. Another factor potentially impacting the long-term stability of the Si55B06 sealant is the presence of metastable pseudowollastonite. Because this phase is only stable above 1125 °C [47], it is likely to undergo a transformation to the stable wollastonite structure during extended exposure to the lower operating temperatures.

Raman spectroscopy was initially employed in this study to provide *in-situ* insights into the crystallization processes occurring during exposure of the sealants to operating temperatures, as demonstrated in previous work [48]. However, it yielded an unexpected outcome, exhibiting a surprisingly low sensitivity to the crystallization processes identified by XRD and confirmed by SEM and EDS techniques. Despite the significant crystallization observed via these other methods, the Raman spectra showed only subtle changes over the course of the 100-h exposure experiments, even for the rapidly crystallizing compositions

Si52B09 and Si55B06. To ensure the validity of the experimental conditions, the furnace used for these measurements was validated to maintain the target temperature with an accuracy of  $\pm 5$  °C.

While the Raman spectra proved to be insensitive to long-term crystallization, they did accurately reflect the extent of crystallization that occurred upon sealing and during the initial 1-h exposure to the operating temperatures. The spectra for Si58B03 and Si61B00 exhibited prominent peaks that were consistent with previously reported data for the walstromite phase [41]. The Si55B06 spectra showed less pronounced peaks, while Si52B09 displayed only a broad line in the 850–1100 cm<sup>-1</sup> range. This spectral region is associated with vibrations of Si–O bonds in silicate tetrahedra with varying numbers of bridging oxygens (BOs) [39,40]. Deconvolution of this peak in Si52B09 yielded an intensity ratio of  $Q_{Si}^2/Q_{Si}^3 = 0.3/1$ , which is in good agreement with the composition of the initial glasses. Although it did not provide additional insights into the sealant's structural evolution during prolonged exposure, the Raman spectroscopy provided adequate data on the samples after sealing and short exposure.

The unusual insensitivity of the Raman spectra to crystallization occurring at operating temperatures, combined with their adequate reflection of crystallization at sealing temperatures and the relatively low penetration depth of Raman spectroscopy (0.5–1 μm), suggests a significant difference in crystallization kinetics between the sealant's surface layer and its bulk. Specifically, it appears that surface crystallization proceeds at a considerably slower rate than bulk crystallization at the operating temperature. This represents a novel insight into the crystallization behavior of SOFC sealants, derived from the combined application of Raman spectroscopy, XRD, and SEM techniques. Further investigation into the spatial distribution of crystallization within bulk sealants for SOFC applications is therefore of considerable importance from both practical and scientific perspectives.

## 5. Conclusions

The key findings of this study include:

- Isothermal heat treatment induced notable crystallization in all studied sealants, with the exception of Si61B00, starting at 850 °C. The extent of crystallization increased with decreasing B<sub>2</sub>O<sub>3</sub> content. Walstromite was the major crystalline phase. Hexacelsian BaAl<sub>2</sub>Si<sub>2</sub>O<sub>8</sub> was also present as a minor phase in all compositions except Si61B00. Notably, the Si55B06 sealant composition uniquely contained significant quantities of pseudowollastonite;
- Heat treatment simulating sealing and exposure to operating temperatures resulted in markedly different phase compositions. After the 100-h exposure, the high-boron compositions Si52B09 and Si55B06 exhibited extensive crystallization and the formation of a new major phase, itsite (Ba<sub>2</sub>Ca(BSi<sub>2</sub>O<sub>7</sub>)<sub>2</sub>). In contrast, Si58B03 and Si61B00 exhibited only very slight further crystallization, with walstromite as the major phase and only minor hexacelsian present in Si58B03;
- DSC analysis at a fixed heating rate revealed only weakly discernible crystallization heat effects for all investigated sealants, indicating a slow crystallization rate;
- *In-situ* Raman spectroscopy measurements were insensitive to crystallization during long-term exposure of the sealants to operating temperatures. Combined analysis by XRD and Raman spectroscopy data indicates that surface crystallization proceeds at a considerably slower rate than bulk crystallization.

Based on the crystallization data obtained in this study for 0.17BaO-0.17CaO-0.05Al<sub>2</sub>O<sub>3</sub>-(0-0.09)B<sub>2</sub>O<sub>3</sub>-(0.61-0.52)SiO<sub>2</sub> compositions, higher-boron sealant compositions may have limited applicability in SOFC systems due to their propensity for extensive crystallization and the formation of continuous crystalline regions within the bulk material.

Conversely, lower-boron compositions appear more promising for SOFC applications from both a thermomechanical compatibility and long-term stability perspective.

### CRedit authorship contribution statement

**Andrey O. Zhigachev:** Writing – original draft, Supervision, Investigation, Conceptualization. **Irina I. Zverkova:** Methodology, Investigation, Formal analysis. **Denis S. Katrich:** Writing – original draft, Investigation. **Nailya S. Saetova:** Visualization, Investigation, Data curation. **Sergey I. Bredikhin:** Supervision, Project administration, Funding acquisition, Conceptualization.

### Declaration of competing interest

The authors declare that they have no known competing financial interests or personal relationships that could have appeared to influence the work reported in this paper.

### Acknowledgements

This work was funded Russian Scientific Foundation (RSF) grant 24-79-10211. The authors thank Alexeeva M.A. from ISSP RAS for help with the samples preparation. Authors acknowledge support of the Research Facility Center at ISSP RAS in the X-ray diffraction studies.

### References

- Mekhilef S, Saidur R, Safari A. Comparative study of different fuel cell technologies. *Renew Sustain Energy Rev* 2012;16:981–9. <https://doi.org/10.1016/j.rser.2011.09.020>.
- Laosiripojana N, Wiyaratn W, Kiatkittipong W, Arpornwichanop A, Sootitiantawat A, Assabumrungrat S. Reviews on solid oxide fuel cell technology. *Eng J* 2009;13:65–84. <https://doi.org/10.4186/ej.2009.13.1.65>.
- Mehrpooya M, Sadeghzadeh M, Rahimi A, Pouriman M. Technical performance analysis of a combined cooling heating and power (CCHP) system based on solid oxide fuel cell (SOFC) technology – a building application. *Energy Convers Manag* 2019;198:111767. <https://doi.org/10.1016/j.enconman.2019.06.078>.
- Singh M, Zappa D, Comini E. Solid oxide fuel cell: decade of progress, future perspectives and challenges. *Int J Hydrogen Energy* 2021;46:27643–74. <https://doi.org/10.1016/j.ijhydene.2021.06.020>.
- Minh NQ. Ceramic fuel cells. *J Am Ceram Soc* 1993;76:563–88. <https://doi.org/10.1111/j.1151-2916.1993.tb03645.x>.
- Kaur G. Thermodynamics, Performance, and configurations of SOFC in: solid oxide fuel cell components. Cham: Springer International Publishing; 2016. p. 123–48. [https://doi.org/10.1007/978-3-319-25598-9\\_4](https://doi.org/10.1007/978-3-319-25598-9_4).
- Blum L, Deja R, Peters R, Stolten D. Comparison of efficiencies of low, mean and high temperature fuel cell systems. *Int J Hydrogen Energy* 2011;36:11056–67. <https://doi.org/10.1016/j.ijhydene.2011.05.122>.
- Carrette L, Friedrich KA, Stimming U. Fuel cells: principles, types, fuels, and applications. *ChemPhysChem* 2000;1:162–93. [https://doi.org/10.1002/1439-7641\(20001215\)1:4<162::AID-CPHC162>3.0.CO;2-Z](https://doi.org/10.1002/1439-7641(20001215)1:4<162::AID-CPHC162>3.0.CO;2-Z).
- Janardhanan VM, Heuveline V, Deutschmann O. Performance analysis of a SOFC under direct internal reforming conditions. *J Power Sources* 2007;172:296–307. <https://doi.org/10.1016/j.jpowsour.2007.07.008>.
- Shiratori Y, Oshima T, Sasaki K. Feasibility of direct-biogas SOFC. *Int J Hydrogen Energy* 2008;33:6316–21. <https://doi.org/10.1016/j.ijhydene.2008.07.101>.
- Elharati MA, Dewa M, Bkour Q, Hussain MA, Miura Y, Dong S, Fukuyama Y, Dale N, Marin-Flores OG, Ha S. Internal reforming solid oxide fuel cell system operating under direct ethanol feed condition. *Energy Technol* 2020;8:2000350. <https://doi.org/10.1002/ente.202000350>.
- Sasaki K, Haga K, Yoshizumi T, Minematsu D, Yuki E, Liu R, Uryu C, Oshima T, Ogura T, Shiratori Y, Ito K, Koyama M, Yokomoto K. Chemical durability of solid oxide fuel cells: influence of impurities on long-term performance. *J Power Sources* 2011;196:9130–40. <https://doi.org/10.1016/j.jpowsour.2010.09.122>.
- Tietz F. Thermal expansion of SOFC materials. *Ionics* 1999;5:129–39. <https://doi.org/10.1007/BF02375916>.
- Xie J, Hao W, Wang F. The analysis of interfacial thermal stresses of solid oxide fuel cell applied for submarine power. *Int J Energy Res* 2018;42:2010–20. <https://doi.org/10.1002/er.4005>.
- Golkhatmi SZ, Asghar MI, Lund PD. A review on solid oxide fuel cell durability: latest progress, mechanisms, and study tools. *Renew Sustain Energy Rev* 2022;161:112339. <https://doi.org/10.1016/j.rser.2022.112339>.
- Dwivedi S. Solid oxide fuel cell: materials for anode, cathode and electrolyte. *Int J Hydrogen Energy* 2020;45:23988–4013. <https://doi.org/10.1016/j.ijhydene.2019.11.234>.
- Ivanov A, Plekhanov M, Kuzmin A. The influence of formation features on SOFC electrochemical performance and long-term stability. *J Appl Electrochem* 2022;52:743–53. <https://doi.org/10.1007/s10800-022-01667-0>.
- Singh K, Wallia T. Review on silicate and borosilicate-based glass sealants and their interaction with components of solid oxide fuel cell. *Int J Energy Res* 2021. <https://doi.org/10.1002/er.7161>.
- Simner SP, Stevenson JW. Compressive mica seals for SOFC applications. *J Power Sources* 2001;102:310–6. [https://doi.org/10.1016/S0378-7753\(01\)00811-4](https://doi.org/10.1016/S0378-7753(01)00811-4).
- Lessing PA. A review of sealing technologies applicable to solid oxide electrolysis cells. *J Mater Sci* 2007;42:3465–76. <https://doi.org/10.1007/s10853-006-0409-9>.
- Singh RN. Sealing technology for solid oxide fuel cells (SOFC). *Int J Appl Ceram Technol* 2007;4:134–44. <https://doi.org/10.1111/j.1744-7402.2007.02128.x>.
- Mahapatra MK, Lu K. Seal glass for solid oxide fuel cells. *J Power Sources* 2010;195:7129–39. <https://doi.org/10.1016/j.jpowsour.2010.06.003>.
- Sohn SB, Choi SY, Kim GH, Song HS, Kim GD. Suitable glass-ceramic sealant for planar solid-oxide fuel cells. *J Am Ceram Soc* 2004;87:254–60. <https://doi.org/10.1111/j.1551-2916.2004.00254.x>.
- Sun T, Xiao H, Guo W, Hong X. Effect of Al<sub>2</sub>O<sub>3</sub> content on BaO–Al<sub>2</sub>O<sub>3</sub>–B<sub>2</sub>O<sub>3</sub>–SiO<sub>2</sub> glass sealant for solid oxide fuel cell. *Ceram Int* 2010;36:821–6. <https://doi.org/10.1016/j.ceramint.2009.09.045>.
- Namwong P, Laorodphan N, Thiemorn W, Jaimasith M, Wannakon A, Chairuangri T. A barium-calcium silicate glass for use as seals in planar SOFCs. *Chiang Mai J Sci* 2010;37:231–42.
- Laorodphan N, Ayawanna J. BaO–Al<sub>2</sub>O<sub>3</sub>–SiO<sub>2</sub>–B<sub>2</sub>O<sub>3</sub> glass-ceramic SOFCs sealant: effect of ZnO additive. *Key Eng Mater* 2017;751:455–60. <https://doi.org/10.4028/www.scientific.net/KEM.751.455>.
- Puig J, Ansart F, Lenormand P, Antoine L, Dailly J. Sol-gel synthesis and characterization of barium (magnesium) aluminosilicate glass sealants for solid oxide fuel cells. *J Non-Cryst Solids* 2011;357:3490–4. <https://doi.org/10.1016/j.jnoncrysol.2011.06.025>.
- Arora A, Singh K, Pandey OP. Thermal, structural and crystallization kinetics of SiO<sub>2</sub>–BaO–ZnO–B<sub>2</sub>O<sub>3</sub>–Al<sub>2</sub>O<sub>3</sub> glass samples as a sealant for SOFC. *Int J Hydrogen Energy* 2011;36:14948–55. <https://doi.org/10.1016/j.ijhydene.2011.03.036>.
- Rezaei N, Ghatte M. Barium-calcium aluminosilicate glass/mica composite seals for intermediate solid oxide fuel cells. *Ceram Int* 2021;47:21679–87. <https://doi.org/10.1016/j.ceramint.2021.04.181>.
- Luo L, Lin Y, Huang Z, Wu Y, Sun L, Cheng L, Shi J. Application of BaO–CaO–Al<sub>2</sub>O<sub>3</sub>–B<sub>2</sub>O<sub>3</sub>–SiO<sub>2</sub> glass-ceramic seals in large size planar IT-SOFC. *Ceram Int* 2015;41:9239–43. <https://doi.org/10.1016/j.ceramint.2015.01.091>.
- Lahl N, Singh K, Singheiser L, Hilpert K, Bahadur D. Crystallisation kinetics in AO–Al<sub>2</sub>O<sub>3</sub>–SiO<sub>2</sub>–B<sub>2</sub>O<sub>3</sub> glasses (A= Ba, Ca, Mg). *J Mater Sci* 2000;35:3089–96. <https://doi.org/10.1023/A:1004851418274>.
- Da Silva MJ, Bartolome JF, Antonio H, Mello-Castanho S. Glass ceramic sealants belonging to BAS (BaO–Al<sub>2</sub>O<sub>3</sub>–SiO<sub>2</sub>) ternary system modified with B<sub>2</sub>O<sub>3</sub> addition: a different approach to access the SOFC seal issue. *J Eur Ceram Soc* 2016;36:631–44. <https://doi.org/10.1016/j.jeurceramsoc.2015.10.005>.
- Lin SE, Cheng YR, Wei WCJ. BaO–B<sub>2</sub>O<sub>3</sub>–SiO<sub>2</sub>–Al<sub>2</sub>O<sub>3</sub> sealing glass for intermediate temperature solid oxide fuel cell. *J Non-Cryst Solids* 2012;358:174–81. <https://doi.org/10.1016/j.jnoncrysol.2011.09.013>.
- Sohn SB, Choi SY, Kim GH, Song HS, Kim GD. Stable sealing glass for planar solid oxide fuel cell. *J Non-Cryst Solids* 2002;297:103–12. [https://doi.org/10.1016/S0022-3093\(01\)01042-0](https://doi.org/10.1016/S0022-3093(01)01042-0).
- Eichler K, Solow G, Otschik P, Schaffrath W. BAS (BaO–Al<sub>2</sub>O<sub>3</sub>–SiO<sub>2</sub>)-glasses for high temperature applications. *J Eur Ceram Soc* 1999;19:1101–4. [https://doi.org/10.1016/S0955-2219\(98\)00382-3](https://doi.org/10.1016/S0955-2219(98)00382-3).
- Zhigachev AO, Alexeeva MA, Bredikhin SI, Tsipis EV, Zverkova II, Agarkova EA. Effect of SiO<sub>2</sub>/B<sub>2</sub>O<sub>3</sub> ratio on high-temperature behavior and crystallization of BaO–CaO–SiO<sub>2</sub>–Al<sub>2</sub>O<sub>3</sub>–B<sub>2</sub>O<sub>3</sub> sealants for SOFCs. *Ceram Int* 2025. <https://doi.org/10.1016/j.ceramint.2025.03.221>.
- Agarkov DA, Burmistrov IN, Tsybrov FM, Tartakovskii II, Kharton VV, Bredikhin SI. Kinetics of NiO reduction and morphological changes in composite anodes of solid oxide fuel cells: estimate using Raman scattering technique. *Russ J Electrochem* 2016;52:600–5. <https://doi.org/10.1134/S1023193516070028>.
- Agarkov DA, Burmistrov IN, Tsybrov FM, Tartakovskii II, Kharton VV, Bredikhin SI. In-situ Raman spectroscopy analysis of the interfaces between Ni-based SOFC anodes and stabilized zirconia electrolyte. *Solid State Ionics* 2017;302:133–7. <https://doi.org/10.1016/j.ssi.2016.12.034>.
- Yadav AK, Singh P. A review of the structures of oxide glasses by Raman spectroscopy. *RSC Adv* 2015;5:67583–609. <https://doi.org/10.1039/C5RA13043C>.
- McMillan PF, Piriou B. Raman spectroscopic studies of silicate and related glass structure: a review. *Bull Mineral* 1983;106:57–75.
- Krzatala A, Krüger B, Galuska I, Vapnik Y, Galuskin E. Walstromite, BaCa<sub>2</sub>(Si<sub>3</sub>O<sub>9</sub>), from rankinite paralava within gehlenite hornfels of the hatrurim basin, negev desert, Israel. *Minerals* 2020;10:407. <https://doi.org/10.3390/min10050407>.
- Galuska IO, Galuskin EV, Vapnik Y, Prusik K, Stasiak M, Dzierzanowski P, Murashko M. Gurimite, Ba<sub>3</sub>(VO<sub>4</sub>)<sub>2</sub> and hexacelsian, BaAl<sub>2</sub>Si<sub>2</sub>O<sub>8</sub> – two new minerals from schorlomite-rich paralava of the Hatrurim Complex, Negev Desert, Israel. *Mineral Mag* 2017;81:1009–19. <https://doi.org/10.1180/minmag.2016.080.147>.
- Kampf AR, Peterson RC, Joy BR. Itsiite, Ba<sub>2</sub>Ca(BSi<sub>2</sub>O<sub>7</sub>)<sub>2</sub>, a new mineral species from Yukon, Canada: description and crystal structure. *Can Mineral* 2014;52:401–7. <https://doi.org/10.3749/canmin.52.3.401>.
- Puig J, Ansart F, Lenormand P, Conradt R, Gross-Barnick SM. Development of barium boron aluminosilicate glass sealants using a sol-gel route for solid oxide

- fuel cell applications. *J Mater Sci* 2016;51:979–88. <https://doi.org/10.1007/s10853-015-9428-8>.
- [45] Aydin B, Toplan HÖ, Toplan N. Non-isothermal crystallization kinetics and properties of CaO-Al<sub>2</sub>O<sub>3</sub>-SiO<sub>2</sub> (CAS) glass-ceramics from eggshell waste, zeolite, and pumice. *Materials* 2024;17:5630. <https://doi.org/10.3390/ma17225630>.
- [46] Walia T, Singh K. Mixed alkaline earth modifiers effect on thermal, optical and structural properties of SrO-BaO-SiO<sub>2</sub>-B<sub>2</sub>O<sub>3</sub>-ZrO<sub>2</sub> glass sealants. *J Non-Cryst Solids* 2021;564:120812. <https://doi.org/10.1016/j.jnoncrsol.2021.120812>.
- [47] Seryotkin YV, Sokol EV, Kokh SN. Natural pseudowollastonite: crystal structure, associated minerals, and geological context. *Lithos* 2021;134–135:75–90. <https://doi.org/10.1016/j.lithos.2011.12.010>.
- [48] Allu AR, Balaji S, Tulyaganov DU, Mather GC, Margit F, Pascual MJ, Siegel R, Milius W, Senker J, Agarkov DA, Kharton VV, Ferreira JM. Understanding the formation of CaAl<sub>2</sub>Si<sub>2</sub>O<sub>8</sub> in melilite-based glass-ceramics: combined diffraction and spectroscopic studies. *ACS Omega* 2017;2:6233–43. <https://doi.org/10.1021/acsomega.7b00598>.